Continuous High-Sensitivity and High-Bandwidth Atomic Magnetometer

Rujie Li,* Fred N. Baynes, André N. Luiten, and Christopher Perrella
Institute for Photonics and Advanced Sensing (IPAS), and School of Physical Sciences, The University of Adelaide, Adelaide, South Australia 5005, Australia

(Received 16 October 2020; accepted 7 December 2020; published 23 December 2020)

Here we demonstrate an atomic magnetometer that has a bandwidth of more than 100 kHz and a sensitivity of 180 fT/$\sqrt{\text{Hz}}$ at a Fourier frequency of 8 Hz, and 0.7 nT/$\sqrt{\text{Hz}}$ at 100 kHz. These sensitivity measurements are achieved at geophysically useful magnetic field magnitudes (approximately 50 μT inside a three-layer μ-metal shield) and are limited by the photon shot noise for frequencies above 8 Hz. This device is based on a nonlinear magneto-optical rotation sensor that is operated with an active feedback to the pump modulation frequency. We present a theoretical description of the response functions of the components in the magnetometer. We show that the range of operation of atomic magnetometers can thus be expanded beyond the conventional high-sensitivity, low-bandwidth domain, to provide a high-linearity, high-bandwidth, and high-sensitivity sensor.

DOI: 10.1103/PhysRevApplied.14.064067

I. INTRODUCTION

Highly sensitive magnetometers find use across a broad swathe of applications, including geophysical exploration [1,2], magnetocardiography (MCG) and magnetoencephalography (MEG) [3–5], detection of nuclear magnetic resonance (NMR), nuclear quadrupole resonance (NQR), and magnetic induction tomography (MIT) [6–9]. The required characteristics of the magnetic sensor depend on the application but frequently cited specifications include sensitivity, linearity, accuracy, bandwidth, slew rate, and dynamic range.

The superconducting quantum interference device (SQUID) is often considered the gold standard magnetic sensor because it delivers simultaneously on many of these requirements, i.e., showing a sensitivity of approximately 1 fT/$\sqrt{\text{Hz}}$ in a wide bandwidth (from a few Hz to several MHz) [10–12] as well as a slew rate of 10.5 nT/μs [13]. Although SQUIDs can be operated from zero field to more than 100 μT [14], the dynamic range is limited to hundreds of nT [10]. Furthermore, SQUIDs detect magnetic flux through a coil, which requires knowledge about the coil area to calculate magnetic field strength, which makes SQUIDs not intrinsically accurate devices [15,16]. Of course, the key downside of SQUID technology is the need to operate it in a cryogenic environment.

In recent times, there have been significant advances in atomic magnetometers (AMs), which now allow them to achieve a competitive sensitivity to that of SQUIDs but without the need of bulky cryogenic cooling systems [17,18]. Nonetheless, AMs have been conventionally considered to be relatively low-bandwidth devices and thus thought to not be competitive in magnetometer applications, which call for a highly dynamic response [19].

As an example, AMs based on Bell-Bloom or M_x interrogation, which have been studied for more than half a century, are capable of working in geophysically interesting magnetic fields (approximately 50 μT) where they show a picoTesla-level sensitivity. However, the fastest of these have shown a bandwidth of several kHz [20–22]. Using continuous quantum nondemolition measurements, Shah *et al.* reported a 1.9-kHz measurement bandwidth, a fourfold improvement compared to the demolition measurement, without sensitivity loss at higher frequencies [23]. AMs in the spin-exchange relaxation-free (SERF) regime can show a sensitivity that is even higher than a SQUID, but this comes at the cost of very narrow bandwidth (approximately 20 Hz) [24–26] and operation in very low fields (typically, less than 10 nT) [27]. Finally, AMs based on nonlinear magneto-optical rotation (NMOR), pioneered by Budker *et al.* and Gawlik *et al.* [28,29], show very high sensitivity and can operate in ambient magnetic fields [30]. In very recent work we have shown that these devices can have a very high bandwidth [31]. This was achieved by direct phase measurement of the Larmor rotation following a strong optical pumping pulse. Although possible to achieve a very high measurement duty cycle, it is not possible to obtain a continuous time record from that device because of the requirement to periodically pump the atomic system.

The highest bandwidth to observe the evolution of the spin system while it is in free evolution AMs are around 1 kHz using self-oscillating techniques [32,33].

*rujie.li@adelaide.edu.au

Nonetheless, we note that there is no intrinsic reason for why an AM using NMOR cannot exhibit continuous measurement and high bandwidth with the right protocol. In this work, we demonstrate a technique to achieve just that. Furthermore, we demonstrate that this is achieved while maintaining all of the other excellent attributes of the NMOR approach, i.e., high accuracy, high linearity as well as high dynamic range. This opens up a wide range of alternative applications for the NMOR technique.

In the present work, we make careful measurements of the temporal response of the NMOR readout in response to a change in magnetic field. As described in more detail below, the atomic vapor cell demonstrates a 36-Hz low-pass filter (LPF) characteristic, which is consistent with the relaxation time of the atomic polarization in the cell. Using those measurements, we design a feedback loop that ensures that the optical pumping pulses are frequency locked to the instantaneous Larmor frequency. Through these means we demonstrate a sensor response bandwidth of 100 kHz, which is the highest bandwidth ever measured for an AM. The bandwidth limitation is set by the electronic systems we use and this could be pushed higher with faster electronic components. The measured transfer function and sensitivity of the device agree well with theoretical modeling. For magnetic measurements, at the geophysically useful level of 50 μT (currently inside a three-layer μ-metal shield), we demonstrate a sensitivity of 180 fT/$\sqrt{\text{Hz}}$ around 8 Hz and 0.7 nT/$\sqrt{\text{Hz}}$ at 100 kHz. This same sensor demonstrates a slew rate of approximately 91.4 nT/μs, which is an order of magnitude higher than the best result reported using SQUIDs [13].

II. OPERATING PRINCIPLES

An alkali atom in a magnetic field [$B(t)$] will experience an energy splitting, $\hbar\Omega_L$, between its Zeeman ground states. Here Ω_L is the Larmor frequency, which is equal to $\gamma B(t)$, where γ is the gyromagnetic ratio of the atomic spins. The Larmor frequency is strictly proportional to the instantaneous value of the magnetic field. In AM, a pump light [30,31] or a rf field [7] is used to produce the coherence between these Zeeman states. The temporal evolution of this coherence can be observed through the modulated absorption or polarization of an additional probe beam—the observed modulation frequency is equal to the Larmor frequency (or its harmonics) thus allowing measurement of the ambient magnetic field.

In conventional AM, modulated pump light with a modulation frequency of Ω_P, which is the technique employed in our experiment, or a rf field with a frequency of Ω_P [7] is applied to find the Larmor frequency. One observes a very strong resonant response in the average polarization of an ensemble of atoms when $\Omega_P = \kappa\Omega_L$, where κ is an integer associated with the rank of the atomic spin polarization moment causing the optical rotation [34]. For NMOR $\kappa = 2$ is generally used, which is the case explored here. Following each pumping pulse, one observes a relaxation of the coherence with a time constant, τ, that is induced by the general relaxation of the atoms, including destructive collisions between the atoms and the cell wall, spin destructions between the atoms as well as the decoherence effect due to the gradient of the magnetic field, etc. This combination of relaxation and pumping gives rise to a Lorentzian-shaped frequency response of the atomic polarization around the Larmor frequency. Active feedback [22], or self-oscillation techniques [32,33], can be used to ensure that Ω_P automatically tracks the Larmor frequency, or its harmonics.

In this paper we design a feedback system that allows us to have a very high bandwidth—here we make use of the protocol outlined in our previous work [31] where it is shown that the instantaneous phase of the polarization rotation of a probe beam responds at a rate that is much faster than the other critical time constants in the system (the Larmor period or the relaxation time). This enables one to build a control system that locks Ω_P onto, in our case 2 Ω_L, with a bandwidth that is much higher than the relaxation time. This is the fastest continuous-output AM yet demonstrated.

III. EXPERIMENTAL DETAILS

An NMOR [28,35] magnetometer is built based on the experimental apparatus shown in Fig. 1. An isotopically enriched sample of ^{87}Rb atoms is contained in a spherical glass vapor cell with a diameter of 40 mm and a temperature of 30 °C. The cell is buffer gas free, paraffin coated to

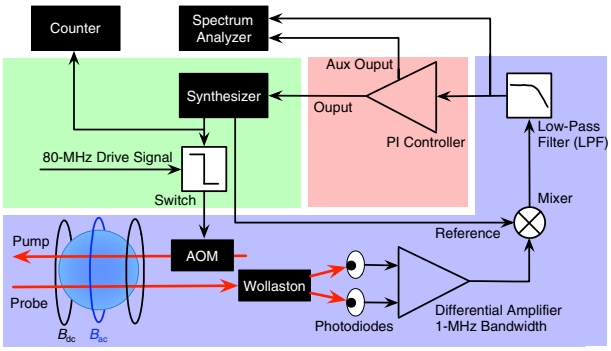

FIG. 1. Experimental diagram of the experimental apparatus used for the magnetic field detection. The sensor, controller, and actuator contained in the closed loop are shaded in purple, pink, and green, respectively. For the open-loop measurement disregarding the proportional-integral (PI) controller, the free-running quadrature signal of the lock-in amplifier based on a mixer is directly read out to test the bandwidth as well as the sensitivity. For the closed-loop test, the PI controller is used to track the changing field (or resonance frequency) via the phase-sensitive detection, and the modulation frequency of the pump beam is counted.

reduce decoherence associated with atom collisions with the cell wall [36,37]. The cell is placed in a three-layer cylindrical magnetic shield (not shown) made of μ-metal, which provides a passive shielding factor of approximately equal to 10^4 to the quasistatic ambient magnetic fields. We use a Lee-Whiting coil pair to provide an average magnetic field, $B_{\rm dc}$, with very small residual gradients in the region of the cell [38]. This magnetic field is aligned along the shield's cylindrical axis. We mount an additional separate pair of coils of just a few turns to deliver a modulated magnetic field, of magnitude $B_{\rm ac}$—this is also aligned along the cell axis.

We pump and probe the atoms with light derived from a distributed Bragg reflector (DBR) laser diode, which is delivered to the cell via fiber optic cables. The laser frequency can be stabilized to any of four hyperfine transitions of the ^{87}Rb $D1$ line using a standard saturated absorption spectroscopy (SAS) setup. The laser light is split into pump and probe beams, both linearly polarized, and then redshifted by 80 MHz by separate acousto-optic modulators (AOM). The pump-beam intensity is 100% modulated by its AOM at a frequency of Ω_P. The average power of the pump beam is 40 μW and it has a $1/e^2$ intensity diameter of 9 mm inside the cell. The probe is a continuous-wave signal with a power of 5 μW and a $1/e^2$ intensity diameter of 1.5 mm. The pump and probe beams counterpropagate through the cell along the z axis. The beam centers of the pump and probe beams are separated by about 11 mm. The intensities and beam sizes of the pump and probe are chosen to maximize the magnetometer's sensitivity.

The polarization rotation of the probe is measured by a balanced polarimeter that is based on a Wollaston prism with two photodiodes monitoring its outputs. A differential amplifier takes the difference of the photodiodes' signal: for small rotations this is proportional to the phase rotation experienced by the probe light in transmission through the cell: $\Delta\phi = (P_1 - P_2)/2(P_1 + P_2)$, where $P_{1,2}$ refers to the power falling on two photodiodes in Fig. 1.

A time-varying magnetic field $B(t)$, which is the sum of ac and dc field components $[B(t) = B_{\rm ac} + B_{\rm dc}]$ shown in Fig. 1, applied to the atomic ensemble leads to an instantaneous spin precession at the Larmor frequency, $\Omega_L(t)=\gamma B(t)$. As the atomic spins rotate in the magnetic field, they impart a sinusoidal modulation to the plane of polarization of the transmitted probe: $\Delta\phi = \phi_{\rm max}\sin[2\ \Omega_L(t)t + \phi_0]$, where ϕ_0 is an initial phase offset. The photodiode signal is synchronously demodulated using a frequency mixer referenced to the pump modulation frequency, Ω_P, with adjustable phase, $\phi_{\rm mixer}$. The mixer is followed by a LPF to eliminate unwanted signals resulting in an output proportional to

$$V_{\rm mixer} = k_{\rm mixer}\sin[2\ \Omega_L(t) - \Omega_P + \phi_0 - \phi_{\rm mixer}], \qquad (1)$$

where $k_{\rm mixer}$ is the sensitivity of the mixer in V/rad.

A. Magnetic field response of NMOR

The relaxation time of the atoms is measured by observing its ring down to be approximately 1.9 ms around 50 μT (see inset in Fig. 2). We can also estimate the relaxation process by measuring the width of the Larmor resonance feature using a nonlinear fit to the NMOR response as a function of pump modulation frequency (see Fig. 2). A sample of the NMOR resonance signals measured at a bias field of 49.2 μT is shown in Fig. 2. The modulation frequency of the pump intensity is swept over 0.8 kHz around the Larmor resonance, and the in-phase (black line) and quadrature (blue line) signals are extracted by the lock-in amplifier. Three Δm=2 coherences are observed for the F_g=2→F_e=1 transition of ^{87}Rb, displayed as the dashed lines in Fig. 2, due to the five Zeeman levels of the $F_g = 2$ ground state. Each component has a 36-Hz HWHM, while the separation between adjacent resonances is due to nonlinear Zeeman splitting ($\delta_{\rm NLZ}$), which we measure to be 68.1 Hz in excellent agreement with that theoretically expected 69.7 Hz at 49.22 μT. An examination of the linewidth of the Larmor resonance as a function of

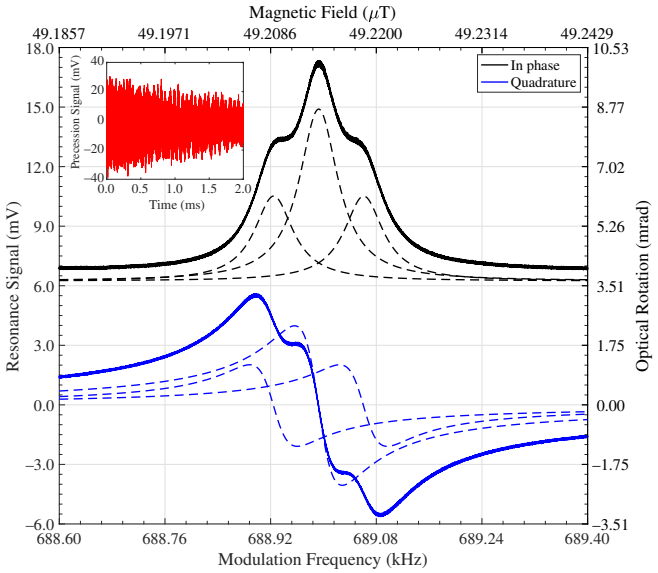

FIG. 2. NMOR resonance signals measured at a bias field of 49.2 μT. The corresponding magnetic field of the modulation frequency is displayed on the top axis, while the quadrature signal is also converted into the rotation angle shown on the right axis. Via curve fitting (not shown), three $\Delta m = 2$ coherences contained in the resonance signals of the $F_g = 2 \rightarrow F_e = 1$ transition can be obtained and are displayed as the dashed lines. Each of the components has a 35.9-Hz HWHM and the separation between them is 68.1 Hz. Unlike other data shown in the following figures, a lock-in amplifier (Model MFLI from ZI), rather than a mixer displayed in Fig. 1, is used to simultaneously acquire the in-phase and quadrature components. To make these curves clear, the in-phase signals are intentionally shifted by 6 mV. Inset: the ring-down signal of Larmor precession in the time domain after the pump is blocked.

incident light powers and magnetic field shows that at magnetic fields larger than 19 μT the broadening is determined by a homogenous broadening associated with small residual magnetic gradients (approximately 0.3 μT/m) within the cell volume [39].

A passive measurement of the frequency response of the NMOR readout technique is achieved by using the linear region of the central quadrature signal (shown on Fig. 2) to translate the magnetic field to a measurable signal. The magnetic field is modulated by applying an ac field to the ac coils. For these experiments, we deliver magnetic field modulation with an amplitude of 1.3 nT on an average field of 50 μT that is supplied by the Lee-Whiting coils. The pump modulation frequency, Ω_P, is tuned to the average Larmor resonance frequency, 2 Ω_L. The ac field amplitude is chosen so that the mixer readout remains in the linear region of the quadrature component.

The open-loop response of the magnetometer is shown as the red crosses in Fig. 3. We fit the data (green line in Fig. 3), which yields a low-frequency response, K_0, of 2.7 mV/nT with a cut-off frequency, ω_c, of $2\pi \times 36.4$ Hz. This agrees well with the resonance linewidth obtained from the frequency-domain measurement shown on Fig. 2. The NMOR response can be effectively modeled in standard Laplace notation as a LPF:

$$G_{\text{sens}}(s) = K_0 \frac{\omega_c}{s + \omega_c}. \tag{2}$$

B. Active magnetometer

The magnetic field dynamic range of the simple NMOR approach described above is limited to the linear range of the dispersive signal shown on Fig. 2, which is around 2 nT. Further, the bandwidth of the magnetometer response is essentially limited to the reciprocal of the relaxation time of the sample. As shown in Refs. [24,40], the sensitivity of a magnetometer is inversely proportional to the relaxation time and hence one finds that most high-sensitivity magnetometers will have a low bandwidth if operated with that approach.

In order to expand the dynamic range, increase linearity and maximize slew rate, and expand the bandwidth of the sensor, the device can be operated in a closed-loop configuration. In this field-tracking state, we actively tune Ω_P to hold the phase difference between Ω_P and 2 Ω_L at zero as measured at the output of the mixer. This is effectively a phase-locked loop, which is locking the phase of the oscillator that generates the pump-pulse stream to the instantaneous phase of the Larmor precession (which can be considered as the second oscillator in the phase lock), observed by the plane of polarization rotation of the probe.

A block diagram of the phase-sensitive feedback technique is shown in Fig. 4. The magnetometer sensor consists of the atomic cell, optical interrogation, and synchronous

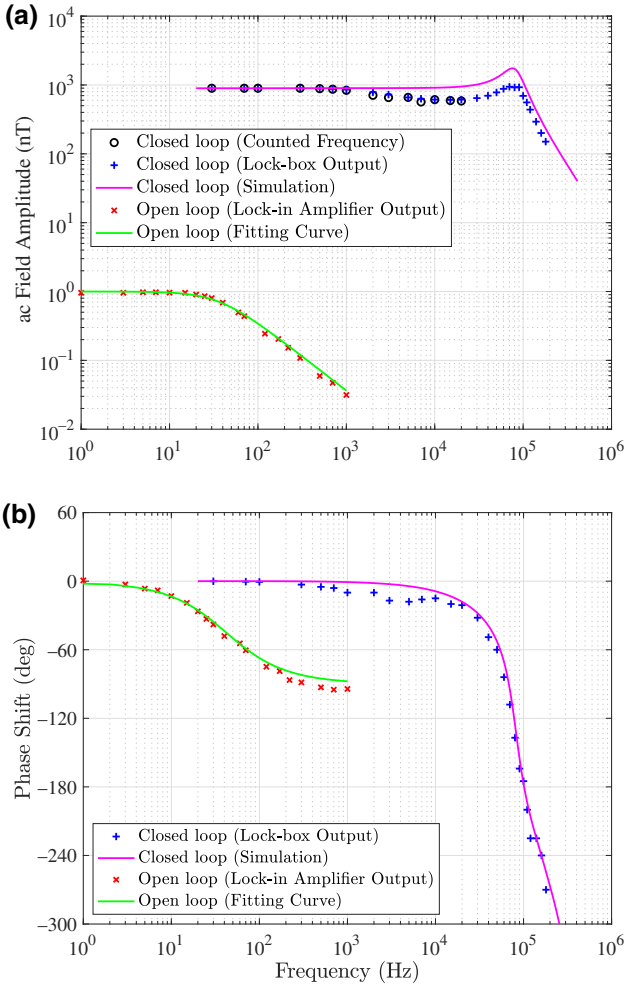

FIG. 3. Amplitude (top) and phase (bottom) responses of the NMOR magnetometer to ac fields. The red crosses represent the amplitude response to ac fields with an amplitude of 1.3 nT for open-loop measurement while the green denotes a fitting curve to $a/\sqrt{f^2 + b^2}$, where the bandwidth $b = 36.4$ Hz. The black circles (from counter) and blue markers (from PI controller) indicate the responses to ac fields with an amplitude of 896 nT for the closed-loop measurement, 700 times stronger than the fields used in the open-loop test. The pink curves are the simulation results based on Eq. (5). The phase of the magnetometer response is delayed by 180° compared to the input field at 100 kHz.

detection as measured and described in the earlier section. A preamplifier and a LPF with a cut-off frequency of 170 kHz are also implemented to extract the weak rotation signal. These are modeled with a transfer function of $G_{\text{gain}}(s)$ and $G_{\text{LPF}}(s)$, respectively, as shown in Fig. 4. The controller is a standard PI filter, which processes the output of the mixer to generate a signal for the actuator. The actuator, a voltage controlled oscillator (VCO), takes the controller signal as an output and delivers two phase synchronous outputs: one sinusoidal output that is used to drive the mixer, and a second pulsed output that is used to chop the pump pulses.

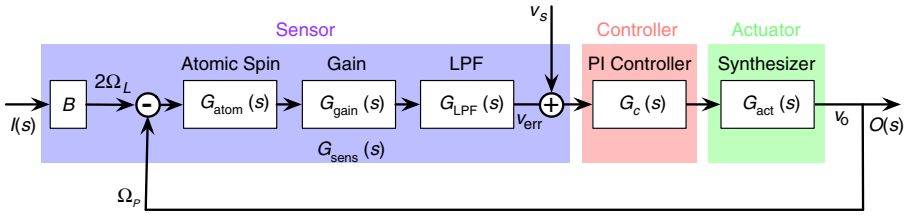

FIG. 4. Block diagram of the elements used in the phase-sensitive feedback technique. The sensor, controller, and actuator contained in the closed loop are shaded in purple, pink, and green, respectively. For the open-loop measurement disregarding the PI controller, the free-running quadrature signal of the lock-in amplifier based on a mixer is directly read to test the bandwidth as well as the sensitivity. For the closed-loop test, the PI controller is used to track the changing field (or resonance frequency) via the phase-sensitive detection, and the modulation frequency of the pump beam is counted. The arrow v_s, which represents the sensor's noise at the output of mixer (or lock-in amplifier) in Fig. 1, is used to analyze its influence on the magnetic noise floor in the closed-loop system, marked as v_o.

An ideal actuator transforms the controller signals into a frequency shift with a flat transfer function; however, the VCO used in our experiment can be best described as an ideal VCO with an internal delay. The response of the VCO is measured by applying a known frequency modulation and comparing the VCO's frequency-modulated output with that of the external modulation. The measured transfer function can be described as

$$G_{\rm act}(s) = K_{\rm VCO} e^{-s\tau_{\rm delay}}, \tag{3}$$

where $\tau_{\rm delay}$ is the measured time delay of 1.3 μs, and $K_{\rm VCO}$ is the low-frequency response of the VCO, which is measured to be 40 kHz/V.

The response of the PI controller is expressed as

$$G_c(s) = K_c + \frac{2\pi f_{\rm PI} K_c}{s}, \tag{4}$$

where K_c is the gain of the controller and $f_{\rm PI}$ is the PI corner frequency. In this case, for optimal performance, we determine that the breakpoint should be set at 30 Hz.

Combining each of the responses from the sensor, controller, and actuator gives the transfer function of the magnetometer in field-tracking mode as [41]

$$H(s) = \frac{G_{\rm sens}(s) G_c(s) G_{\rm act}(s)}{1 + G_{\rm sens}(s) G_c(s) G_{\rm act}(s)}, \tag{5}$$

which is used to compare to experimental results in Fig. 3.

IV. CLOSED-LOOP RESPONSE

To confirm the expected closed-loop response we experimentally evaluate the response of the magnetometer to an oscillating magnetic field. As with the earlier measurements of the NMOR sensor, we superimpose an ac field on the 50 μT bias field. In this case, we explore a much wider range of frequencies varying from 1 Hz up to 180 kHz.

The response of the magnetometer to the changing magnetic field is estimated in two separate ways (see Fig. 1). For applied magnetic modulation frequencies from 30 Hz–10 kHz we directly measure the pump frequency, Ω_m, using a frequency counter [open circles on Fig. 3(a)]. We also measure the feedback signal to the VCO using a spectrum analyzer [crosses on Fig. 3(a)] for frequencies in the range of 30 Hz–200 kHz.

We see on Fig. 3 that there is good agreement between the simulation using the individual transfer functions of the components in Eq. (5) and the overall response of the closed-loop magnetometer. A factor of 1.5 discrepancy between the simulation and measurements is seen above 2 kHz. This is attributed to the ac field generated by the ac coil being partially canceled by the dc coil through electromagnetic induction at high frequencies.

The experimental transfer functions show that the bandwidth is expanded to 100 kHz under the locked state, Fig. 3(a). This is more than 3 orders of amplitude greater than that of the open-loop condition, and 1 order higher than the result measured at 11.4 μT reported by Jiménez-Martínez *et al.* [19]. A flat-phase response is observed up to 10 kHz, above which the pump frequency phase lags the atomic response resulting in a 180° phase lag at 100 kHz. This phase lag is predominately caused by the 1.3 μs time delay in the VCO. We thus emphasize that the current 100-kHz limit is not set by the atoms, but instead by technical limits in the electronics. An improvement in the characteristics of the VCO could increase the bandwidth by an additional amount.

We note that the actively locked magnetometer has a much larger dynamic range than the open-loop device: as an example of this, the response function of the magnetometer is obtained on Fig. 3 using an ac field that had an amplitude of 900 nT. This is 700 times larger than that measured through the simple approach described in Sec. III A.

As another measure of the dynamic and linear response of the magnetometer we test its slew rate. Compared to the increased bandwidth achieved in open loop via adding a frequency-dependent gain at the sensor output, the closed-loop technique shown here allows continuous

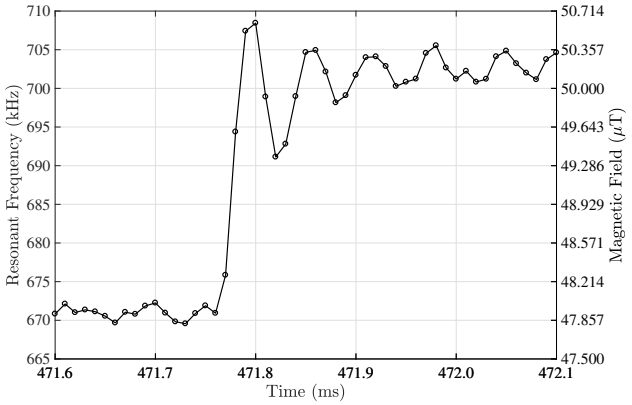

FIG. 5. Measurement of the slew rate. Under the field-tracking state, a sudden change in the field ($\Delta B = 2.286\ \mu$T) with a rising edge of 30 ns is applied to the NMOR magnetometer and its response (modulation frequency of pump beam) is read by a counter. The magnetometer response shown here gives a slew rate of 91.4 nT/μs.

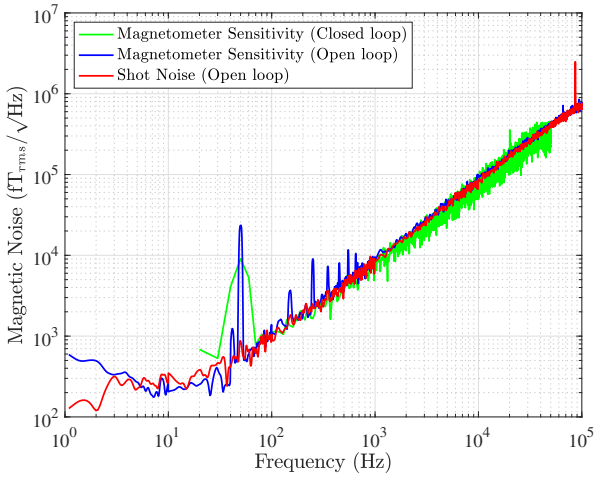

FIG. 6. Magnetic noise floor of NMOR system. The blue line is the normalized sensitivity for the open-loop measurement, while the red line is the photon shot noise. The green line, which is calculated based on the PSD of the resonance frequency from the counter in Fig. 1, indicates the noise floor in the field-tracking mode. The closed-loop data agrees very well with the open-loop result, and a sensitivity of 180 fT/$\sqrt{\text{Hz}}$ has been obtained around 8 Hz at 50 μT.

measurement of the field even when the field strength changes by more than the Larmor linewidth as the pump modulation is always on resonant with twice the Larmor frequency. An example is shown in Fig. 5 in which a sudden (driving-coil voltage rise time is approximately 30 ns) and relatively large ($\Delta B \sim 2.286\ \mu$T) change is made in the magnitude of the magnetic field at the cell. The measured slew rate is 91.4 nT /μs, which is approximately 10 times higher than that of SQUIDs [13]. As can be seen in Fig. 5, there is ringing in the control loop after the step change in magnetic field, which arises from the peaking in the amplitude response of the transfer function seen in Fig. 3(a). The undesirable overshoot and oscillation effects can be suppressed by an adjustment of the control system that focuses on a flatter response at the expense of maximum bandwidth. Alternatively, a VCO with a smaller inherent delay can equally assist in removing this undesirable characteristic.

V. FREQUENCY-DEPENDENT SENSITIVITY

It is important to measure the sensitivity of a magnetometer over a range of frequencies, which are applicable to its use. However, we note that this measurement is quite subtle and a simple approach can yield results that are misleading. In the absence of any external magnetic noise, for example, in the closed-loop magnetometer, we observe a voltage noise at the output of mixer, which is close to white, while the magnetic response is also observed to be flat over an extended range of frequencies (as we show here). This can create the false impression that the magnetic sensitivity of the device is also white. As we show here, this is not correct.

To measure the magnetometer sensitivity in both the open- and closed-loop cases, the ac magnetic field is turned off and the noise of the magnetometer is measured in a very quiet and constant field of 50 μT. To obtain a measurement of the residual fluctuations in the open-loop configuration, we directly sample the output of the mixer using a spectrum analyzer. In order to translate these voltage fluctuations into magnetic field fluctuations it is necessary to take into account the response of the sensor, G_{sens} [see Fig. 3(a)]. The resulting magnetic sensitivity is plotted in blue in Fig. 6 and shows a characteristic shape that it is relatively flat up to the bandwidth of the Larmor resonance, and then degrades proportional to the Fourier frequency when higher than that bandwidth. Numerically, we observe a sensitivity of 180 fT/$\sqrt{\text{Hz}}$ around 8 Hz and 0.7 nT$\sqrt{\text{Hz}}$ at 100 kHz at the bias field of 50 μT. We independently estimate the impact of photon shot noise on the photodiodes by measuring the photocurrent. Similarly to the sensitivity curve in Fig. 6, the normalized shot noises, displayed by the red trace on Fig. 6, also grow as a function of frequency due to G_{sens}. We see that the magnetometer is shot noise limited above 8 Hz. At low frequencies, drifts in the magnetic environment of the cell result in additional noise. At 8 Hz, the dominant photon shot noise is measured to be 163 fT/$\sqrt{\text{Hz}}$, while the thermal noise of the shields is predicted to be around 9.2 fT/$\sqrt{\text{Hz}}$ [42]. The current noise in the field coil can also contribute to the measurement throughout the frequencies, but it is hard to distinguish it from the noise of the shields. Of course, this noise source should not be thought of as noise of the magnetometer itself but instead a limitation associated with the quietest magnetic environment that it is possible to create. While the coils and shields

are necessary to remove the magnetic noise of the laboratory environment, they would not be present in real-world sensing applications.

The magnetic sensitivity of the closed-loop magnetometer configuration is evaluated under the same external conditions as the simple sensor configuration, but instead we measure the residual noise by counting the frequency fluctuations of the pump modulation (Ω_P). The power spectral density of these frequency fluctuations are shown in green in Fig. 6. And the high-bandwidth closed-loop device shows a sensitivity that is identical to the relatively slow open-loop measurement.

The explanation for this can be found in a noise analysis of the control loop in Fig. 4. To facilitate the intrinsic noise analysis of magnetometer system operated in the closed-loop mode (locked state), we assume the external field (or 2 Ω_L) acts as a constant, and the noise of the sensor at the output of mixer is marked as v_s, shown in Fig. 4. And v_s is independent of atomic responses. Analyzing the transmission of the noise in the block diagram [43], we get the following equations:

$$v_{\text{err}} = -v_o G_{\text{sens}}(s), \tag{6}$$

$$v_o = (v_{\text{err}} + v_s) G_c(s) G_{\text{act}}(s), \tag{7}$$

for the electronic noises at the output of the mixer and output of the actuator in the tracking mode, respectively.

Solving for the noise at the output, v_o, in Eqs. (6) and (7) gives the following expressions:

$$\begin{aligned} v_o &= \frac{G_c(s)G_{\text{act}}(s)}{1 + L(s)} v_s \\ &= \frac{L(s)}{1 + L(s)} \frac{1}{G_{\text{sens}}(s)} v_s, \end{aligned} \tag{8}$$

where $L(s) = G_{\text{sens}}(s)G_c(s)G_{\text{act}}(s)$. If the gain is high enough, such that $L(s) \gg 1$, Eq. (8) can be simplified into

$$v_o \approx \frac{1}{G_{\text{sens}}(s)} v_s, \tag{9}$$

which describes the transmission of the sensor's noise in the field-tracking mode and is used to compare to experimental results in Fig. 6. The term on the right side of Eq. (9) is inversely proportional to the open-loop transfer function, $G_{\text{sens}}(s)$, which responds as a low-pass filter, thus the sensor noise (v_s) will be amplified at frequencies above the filters cut-off frequency with a gain proportional to the noises' Fourier frequency, f. For example, if the sensor's noise at the output of mixer is white, as is the situation when limited by photon shot noise, magnetic noise above the cut-off frequency will increase proportional to f. This noise amplification can be understood from two different perspectives. Considering that the sensor acts as a LPF, the signal response from the sensor decreases with increasing f reducing the SNR above the LPF cut-off frequency, f_c. As the control loop will act to maintain Ω_m=2Ω_L and maximize the signal output of the magnetometers, in other words, it acts to keep the output of the magnetometer constant, the decreasing SNR at high Fourier frequencies will increase the magnetic noise floor when locked.

A second way of understanding the increase in magnetic noise at high frequencies is by interpreting the function of the magnetometer when below and above f_c. Note that a white noise at the output of mixer implies a white phase noise at the output of the differential photodiodes, which detect the oscillating Larmor precession. And the magnetic noise in the close loop scales proportionally with the frequency noise of the oscillation signal. For noise Fourier frequencies below f_c, the frequency noise plays a more important role in the frequency (or filed) tracking. And the frequency noise appears directly at the output of the control loop. For noise Fourier frequencies above f_c, the white phase noise governs the frequency tracking. In this case, the phase noise is converted into frequency noise by the controller and actuator. The process of phase-to-frequency conversion introduces an integration term such that

$$v_o\,(f\ > f_c) = \int_{f_c}^{\infty} v_s\, df\,, \tag{10}$$

which if the sensor noise are a simple function such that $v_o \propto f^{\,n}$, where n is a real number, then

$$v_o\,(f\ > f_c) = v_s(f\,)\frac{f}{n+1}. \tag{11}$$

The second term of Eq. (9) reduces to that of Eq. (11) for $f > f_c$ when expressed in the frequency domain. For a white phase noise, due to the shot noise on the detectors, greater frequency noises would be observed above f_c [44].

It is interesting to understand the impact on the performance of a magnetometer if we are to increase or decrease the relaxation of the atomic polarization. To simplify the analysis and make an easy experimental verification, here we consider a special case. Assuming most of the experimental conditions (for example, the atom density, the pump and probe powers, etc.) are kept the same but the atom lifetime is prolonged by N times via improving the coating quality or the residual gradients, the linewidth of NMOR spectra will become N-time narrower while the amplitude will become N-fold greater. Therefore, the slope of central part of the quadrature component (or the scale factor) will get N^2 times steeper (greater). The magnetic noise floor within the bandwidth can be directly improved by a factor of N^2, as the low-frequency voltage noise after the mixer remains the same. However, only an improvement factor of N is

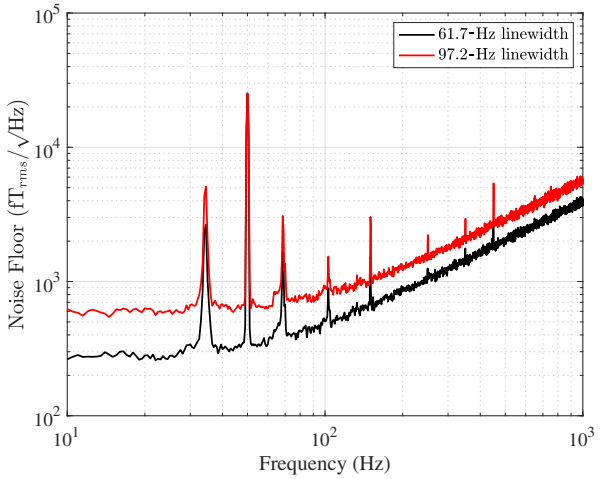

FIG. 7. Sensitivity comparison under different linewidths. When the linewidth is 61.7 Hz, a sensitivity of 282 (4027) fT/$\sqrt{}$Hz is obtained at 20 (1000) Hz. For comparison, a sensitivity 606 (5759) fT/$\sqrt{}$Hz is achieved at 20 (1000) Hz with a linewidth of 97.2 Hz. The broadened linewidth is realized by intentionally worsening the gradient but without changing other parameters.

expected for the magnetic noise level outside the bandwidth, because another factor of N is canceled by N-fold higher normalized voltage noise, expressed in Eq. (9), due to the narrower bandwidth. A comparison of the noise floor obtained at 61.7 and 97.2 Hz is shown in Fig. 7. Compared to the noise floor measured with a 97.2 Hz linewidth, the sensitivity within (outside) the bandwidth is improved by a factor of 2.15 (1.43) for the case with a linewidth of 61.7 Hz. This agrees with the predicted sensitivity change of 2.48 (1.58) with the discrepancy between experiment and theory due to magnetic noise in the measurement.

VI. DISCUSSION

These experiments have brought forth an interesting analogy between the active magnetometer described above, and that of a much more familiar system—the Pound-Drever-Hall [44] approach to locking a laser to a mode of a high-Q optical cavity [45].

In both cases, one compares the phase of an external oscillator (the laser in the PDH case, and the pump-pulse stream of the magnetometer) against an excitation created in a passive resonator. In the PDH case, this excitation is the circulating field in the mode of the passive resonator, whereas in the case of the magnetometer we observe a spin excitation in an atomic ensemble.

The resonant frequency of the passive element is set by the cavity length in the case of the optical resonator, while in the atomic system this is set by the magnetic field strength and the parameters of the atomic species.

The phase comparison between the external field and the excited resonant field provides an error signal that is used to steer the external field into resonance. As both analogous systems possess internal relaxation mechanisms that are independent of the level of excitation, we see an exponential damping in the time domain. This leads to a Lorentzian-shaped resonance in both cases.

The analogy is perhaps useful in providing a further understanding for why the locking bandwidth in both cases can greatly exceed the bandwidth of the resonance. It also is useful in understanding how an external change in the length of the resonant cavity, or an external change in the magnitude of the magnetic field, can be transduced into a change in the laser frequency or pump modulation frequency at a speed which is much higher than the relaxation of the resonator.

Finally, the residual frequency noise in a PDH laser-locking approach is dominated by a white frequency floor for Fourier frequencies up to the cavity bandwidth, and then demonstrates a worsening performance outside the bandwidth. Similarly, for the magnetometer, as we demonstrate in this Paper, the sensitivity of the device is white inside the bandwidth of the Larmor resonance, and then worsens proportional to the Fourier frequency, outside that bandwidth.

VII. CONCLUSION AND FUTURE WORK

In summary, the bandwidth of an actively locked NMOR magnetometer is studied theoretically and experimentally. This allows us to achieve an extremely fast atomic magnetometer with a bandwidth of up to 100 kHz. This is only limited by technical constraints of the locking electronics. At the bias field of 50 μT, we achieve a sensitivity of 180 fT/$\sqrt{}$Hz around 8 Hz and 0.7 nT$\sqrt{}$Hz at 100 kHz. These sensitivities are only limited by fundamental photon shot noise in the sensor. The frequency-dependent sensitivity of both the open- and closed-loop magnetometers is demonstrated as identical, which is critical for a clear understanding of the performance of practical atomic magnetometers. The characteristic of a worsening sensitivity at higher frequencies is observed and explained. A slew rate of 91.4 nT/μs is demonstrated, which is almost an order higher than that possible with a SQUID-based magnetometer. Our investigation shows that the NMOR magnetometer is able to offer a high-sensitivity field measurement not only for the dc field but also for ac fields with a frequency up to 100 kHz.

This work can also deepen our understanding upon the bandwidth of AMs and open the possibility of a wider application for AMs. In addition, it is also meaningful for the investigations on other atom experiments, for instance, the inertial sensor based on polarized atomic spins [46,47].

ACKNOWLEDGMENTS

The authors sincerely thank A. Dowler at OptoFab Adelaide for assistance in mechanical machining of the experimental components, and N. Wilson for his help with the experiment. This work is performed, in part, at the OptoFab node of the Australian National Fabrication Facility utilizing Commonwealth and SA State Government funding. This research is supported by an Innovation Connections Grant from the Australia Government.

[1] P. Schmidt, D. Clark, K. Leslie, M. Bick, D. Tilbrook, and C. Foley, GETMAG - a SQUID magnetic sensor gradiometer for mineral and oil exploration, Explor. Geophys. **35**, 297 (2004).

[2] M. N. Nabighian, V. J. S. Grauch, R. O. Hansen, T. R. LaFehr, Y. Li, J. W. Peirce, J. D. Phillips, and M. E. Ruder, The historical development of the magnetic method in exploration, Geophysics **70**, 33ND (2005).

[3] E. Boto, N. Holmes, J. Leggett, G. Roberts, V. Shah, S. S. Meyer, L. D. Munoz, K. J. Mullinger, T. M. Tierney, S. Bestmann, G. R. Barnes, R. Bowtell, and M. J. Brookes, Moving magnetoencephalography towards real-world applications with a wearable system, Nature (London) **555**, 657 (2018).

[4] S. Morales, M. C. Corsi, W. Fourcault, F. Bertrand, G. Cauffet, C. Gobbo, F. Alcouffe, F. Lenouvel, M. L. Prado, F. Berger, G. Vanzetto, and E. Labyt, Magnetocardiography measurements with ^{4}He vector optically pumped magnetometers at room temperature, Phys. Med. Biol. **62**, 7267 (2017).

[5] B. Amir, R. C. Tony, D. G. Josh, P. C. Anthony, J. Yuan-Yu, B. Christopher, M. Jim, S. Julia, W. Michael, and D. D. S. Peter, A 20-channel magnetoencephalography system based on optically pumped magnetometers, Phys. Med. Biol. **62**, 8909 (2017).

[6] S.-K. Lee, K. L. Sauer, S. J. Seltzer, O. Alem, and M. V. Romalis, Subfemtotesla radio-frequency atomic magnetometer for detection of nuclear quadrupole resonance, Appl. Phys. Lett. **89**, 214106 (2006).

[7] I. M. Savukov, S. J. Seltzer, and M. V. Romalis, Detection of NMR signals with a radio-frequency atomic magnetometer, J. Magn. Reson. **185**, 214 (2007).

[8] A. Wickenbrock, S. Jurgilas, A. Dow, L. Marmugi, and F. Renzoni, Magnetic induction tomography using an all-optical ^{87}Rb atomic magnetometer, Opt. Lett. **39**, 6367 (2014).

[9] C. Deans, L. Marmugi, S. Hussain, and F. Renzoni, Electromagnetic induction imaging with a radio-frequency atomic magnetometer, Appl. Phys. Lett. **108**, 103503 (2016).

[10] D. Drung, S. Bechstein, K. P. Franke, M. Scheiner, and T. Schurig, Improved direct-coupled dc SQUID read-out electronics with automatic bias voltage tuning, IEEE. Trans. Appl. Supercond. **11**, 880 (2001).

[11] N. Oukhanski, R. Stolz, V. Zakosarenko, and H. G. Meyer, Low-drift broadband directly coupled dc SQUID read-out electronics, Physica C **368**, 166 (2002).

[12] J.-H. Storm, P. Hömmen, D. Drung, and R. Körber, An ultra-sensitive and wideband magnetometer based on a superconducting quantum interference device, Appl. Phys. Lett. **110**, 072603 (2017).

[13] T. Hato, A. Tsukamoto, S. Adachi, Y. Oshikubo, H. Watanabe, H. Ishikawa, M. Sugisaki, E. Arai, and K. Tanabe, Development of HTS-SQUID magnetometer system with high slew rate for exploration of mineral resources, Supercond. Sci. and Technol. **26**, 115003 (2013).

[14] M. Mößle, W. R. Myers, S.-K. Lee, N. Kelso, M. Hatridge, A. Pines, and J. Clarke, SQUID-detected in vivo MRI at microtesla magnetic fields, IEEE. Trans. Appl. Supercond. **15**, 757 (2005).

[15] D. F. He and H. Itozaki, Measuring the absolute magnetic field using high-Tc SQUID, J. Phys.: Conf. Ser. **43**, 1227 (2006).

[16] D. F. He and H. Itozaki, High-Tc dc SQUID readout electronics with low noise and high bandwidth, Physica C: Supercond. Appl. **445-448**, 982 (2006).

[17] H. B. Dang, A. C. Maloof, and M. V. Romalis, Ultrahigh sensitivity magnetic field and magnetization measurements with an atomic magnetometer, Appl. Phys. Lett. **97**, 151110 (2010).

[18] R. J. Cooper, D. W. Prescott, P. Matz, K. L. Sauer, N. Dural, M. V. Romalis, E. L. Foley, T. W. Kornack, M. Monti, and J. Okamitsu, Atomic Magnetometer Multisensor Array for rf Interference Mitigation and Unshielded Detection of Nuclear Quadrupole Resonance, Phys. Rev. Appl. **6**, 064014 (2016).

[19] R. Jiménez-Martínez, W. C. Griffith, S. Knappe, J. Kitching, and M. Prouty, High-bandwidth optical magnetometer, J. Opt. Soc. Am. B **29**, 3398 (2012).

[20] R. Jiménez-Martínez, W. C. Griffith, W. Ying-Ju, S. Knappe, J. Kitching, K. Smith, and M. D. Prouty, Sensitivity comparison of Mx and frequency-modulated bell-bloom Cs magnetometers in a microfabricated cell, IEEE Trans. Instrum. Meas. **59**, 372 (2010).

[21] V. Schultze, R. Ijsselsteijn, T. Scholtes, S. Woetzel, and H.-G. Meyer, Characteristics and performance of an intensity-modulated optically pumped magnetometer in comparison to the classical M_x magnetometer, Opt. Express **20**, 14201 (2012).

[22] C. S. Levy, T. W. Kornack, and P. P. Mercier, Bell-bloom magnetometer linearization by intensity modulation cancellation, IEEE Trans. Instrum. Meas. **69**, 883 (2020).

[23] V. Shah, G. Vasilakis, and M. V. Romalis, High Bandwidth Atomic Magnetometery with Continuous Quantum Nondemolition Measurements, Phys. Rev. Lett. **104**, 013601 (2010).

[24] I. K. Kominis, T. W. Kornack, J. C. Allred, and M. V. Romalis, A subfemtotesla multichannel atomic magnetometer, Nature (London) **422**, 596 (2003).

[25] R. Li, W. Quan, W. Fan, L. Xing, Z. Wang, Y. Zhai, and J. Fang, A dual-axis, high-sensitivity atomic magnetometer, Chin. Phys. B **26**, 120702 (2017).

[26] E. Zhivun, M. Bulatowicz, A. Hryciuk, and T. Walker, Dual-Axis π-Pulse Magnetometer with Suppressed Spin-Exchange Relaxation, Phys. Rev. Appl. **11**, 034040 (2019).

[27] R. Li, W. Quan, W. Fan, and J. Fang, Measurement and cancellation of light shift in optically pumped magnetometers, EPL (Europhysics Letters) **121**, 63001 (2018).

[28] D. Budker, W. Gawlik, D. F. Kimball, S. M. Rochester, V. V. Yashchuk, and A. Weis, Resonant nonlinear magneto-optical effects in atoms, Rev. Mod. Phys. **74**, 1153 (2002).

[29] W. Gawlik, L. Krzemień, S. Pustelny, D. Sangla, J. Zachorowski, M. Graf, A. O. Sushkov, and D. Budker, Nonlinear magneto-optical rotation with amplitude modulated light, Appl. Phys. Lett. **88**, 131108 (2006).

[30] V. Acosta, M. P. Ledbetter, S. M. Rochester, D. Budker, D. F. Jackson Kimball, D. C. Hovde, W. Gawlik, S. Pustelny, J. Zachorowski, and V. V. Yashchuk, Nonlinear magneto-optical rotation with frequency-modulated light in the geophysical field range, Phys. Rev. A **73**, 053404 (2006).

[31] N. Wilson, C. Perrella, R. Anderson, A. Luiten, and P. Light, Wide-bandwidth atomic magnetometry via instantaneous-phase retrieval, Phys. Rev. Res. **2**, 013213 (2020).

[32] P. D. D. Schwindt, L. Hollberg, and J. Kitching, Self-oscillating rubidium magnetometer using nonlinear magneto-optical rotation, Rev. Sci. Instrum. **76**, 126103 (2005).

[33] J. M. Higbie, E. Corsini, and D. Budker, Robust, high-speed, all-optical atomic magnetometer, Rev. Sci. Instrum. **77**, 113106 (2006).

[34] V. V. Yashchuk, D. Budker, W. Gawlik, D. F. Kimball, Y. P. Malakyan, and S. M. Rochester, Selective Addressing of High-Rank Atomic Polarization Moments, Phys. Rev. Lett. **90**, 253001 (2003).

[35] S. Pustelny, PhD dissertation (Jagiellonian University, Krakow, 2007).

[36] G. Singh, P. Dilavore, and C. O. Alley, A technique for preparing wall coated cesium vapor cells, Rev. Sci. Instrum. **43**, 1388 (1972).

[37] M. V. Balabas, D. Budker, J. Kitching, P. D. D. Schwindt, and J. E. Stalnaker, Magnetometry with millimeter-scale antirelaxation-coated alkali-metal vapor cells, J. Opt. Soc. Am. B **23**, 1001 (2006).

[38] J. L. Kirschvink, Uniform magnetic fields and double-wrapped coil systems: Improved techniques for the design of bioelectromagnetic experiments, Bioelectromagnetics **13**, 401 (1992).

[39] S. Pustelny, D. F. J. Kimball, S. M. Rochester, V. V. Yashchuk, and D. Budker, Influence of magnetic-field inhomogeneity on nonlinear magneto-optical resonances, Phys. Rev. A **74**, 063406 (2006).

[40] M. P. Ledbetter, I. M. Savukov, V. M. Acosta, D. Budker, and M. V. Romalis, Spin-exchange-relaxation-free magnetometry with Cs vapor, Phys. Rev. A **77**, 033408 (2008).

[41] S. Haykin and B. V. Veen, in *Signals and Systems* (JOHN WILEY & SONS, INC., New York, US, 1999).

[42] S.-K. Lee and M. V. Romalis, Calculation of magnetic field noise from high-permeability magnetic shields and conducting objects with simple geometry, J. Appl. Phys. **103**, 084904 (2008).

[43] S. A. Frank, in *Control Theory Tutorial - Basic Concepts Illustrated by Software Examples* (Springer, Cham, Switzerland, 2018).

[44] R. W. P. Drever, J. L. Hall, F. V. Kowalski, J. Hough, G. M. Ford, A. J. Munley, and H. Ward, Laser phase and frequency stabilization using an optical resonator, Appl. Phys. B, **31**, 97 (1983).

[45] M. J. Martin and J. Ye, in *Optical Coatings and Thermal Noise in Precision Measurement* (Cambridge University Press, London, 2012).

[46] W. Quan, Y. Li, and B. Liu, Simultaneous measurement of magnetic field and inertia based on hybrid optical pumping, EPL (Europhysics Letters) **110**, 60002 (2015).

[47] R. Li, W. Fan, L. Jiang, L. Duan, W. Quan, and J. Fang, Rotation sensing using a K-Rb-^{21}Ne comagnetometer, Phys. Rev. A **94**, 032109 (2016).